Wing Rock Prediction in Free-to-Roll Motion Using CFD Simulations

Mohamed Sereez,* Caroline Lambert,† Nikolay Abramov,‡ and Mikhail Goman§ 1

1,2 *Coventry University, Coventry, CV1 5FB, United Kingdom*

3,4 *De Montfort University, Leicester, LE1 9BH, United Kingdom*

The free-to-roll wing rock CFD simulation of a slender 80-degree delta wing is performed using the Dynamic Fluid-Body Interaction (DFBI) framework and the overlap/chimera mesh method. The purpose of the simulations carried out was to test the capabilities of the current CFD methods for predicting wing rock motion over a wide range of angles of attack, including strong conical vortex interactions and vortex breakdown phenomenon. The predictions of steady aerodynamic dependencies and the aerodynamic stability derivatives based on forced oscillation tests along with the time histories of the wing rock motion of an 80-degree delta wing are in good qualitative and quantitative agreement with the available wind tunnel experimental data demonstrating onset of the wing rock motion. At higher angles of attack with vortex breakdown CFD simulations demonstrated an excitation of the large amplitude regular oscillations or the low amplitude chaotic oscillations depending on the applied initial conditions.

I. Introduction

The aerodynamics of combat aircraft at high angles of attack, performing steady and maneuverable flight, has been studied for decades, and now there is a significant amount of knowledge and information in this area obtained from experimental testing and computational modeling [1]. Recently, a better understanding of the aerodynamics at high angles of attack of modern transport aircraft has become critical due to the problem of loss of control in flight (LOC-I) and the need for aircraft Upset Prevention and Recovery Training (UPRT) by pilots in flight simulators [2].

The aerodynamics of high angles of attack is greatly influenced by the development of separation and vortex flow structures, leading to various aperiodic and oscillatory modes of aircraft unstable motion in the stall area [3]. The aircraft self-sustained oscillations in the lateral-directional motion quite typical for many aircraft configurations attracted a lot of research efforts. Significant amount of experimental and computational works was focused on investigation of aerodynamic phenomena and dynamics of slender delta wings moving only in roll or in so called free-to-roll motion [4–14].

---

*Lecturer (Assistant), School of Future Transport Engineering, MRAeS

†Associate Professor of Aerospace Engineering, School of Future Transport Engineering, MRAeS, SFHEA

‡Senior Lecturer, School of Engineering and Sustainable Development

§Professor of Dynamics, School of Engineering and Sustainable Development, FRAeS

Experimental studies allowed to identify major aerodynamic sources of self-induced oscillations in roll of slender delta wings named as wing-rock. In great extent, wing-rock is driven by leading edge conical vortices which delay in time with respect to their positions and circulation in static conditions causing destabilising effects [4–7, 10, 11]. The breakdown of the leading edge vortices with increase of angle of attack due to negative pressure gradients in the vicinity of trailing edge brings additional nonlinear effects leading to a break of symmetry in the wing equilibrium position [12].

Computational studies of wing-rock oscillations have also been quite successful, moving from using low-order models to more sophisticated approaches [8, 13, 14]. A simplified modelling based on the Brown-Michael formulation for the leading edge vortices clearly revealed a mechanism of sustainable limit cycle wing rock oscillations due to the changing negative damping effect at low oscillation amplitudes to stabilising positive damping at higher oscillation amplitudes giving a balance of energy in wing rock [8, 15]. An approach based on using the Euler equations for modelling conical vortices with no account for vortex breakdown phenomenon has demonstrated a comprehensive flow field parameters underlying self-induced wing rock motion [13]. A promising development in fast prediction of the wing rock onset based on the URANS equations discretized model in the form of ODE for flow parameters on a mesh and rigid body variables have been considered in [14] and in [16]s.

In this paper, wing rock simulation in free-to-roll motion for an 80-degree delta wing is performed using the URANS equations for a wide range of angles of attack using Star-CCM+ CFD code [17] and an overset mesh approach which had shown a robust performance for various complex aerodynamic flows as in [18]. This range includes the development of leading edge vortices with increasing intensity, as well as the phenomenon of vortex breakdown, leading to the emergence of two asymmetric equilibrium positions. To indicate the onset of the wing rock oscillations mathematically described by the so called Hopf bifurcation for onset of limit cycle oscillations [3], low-amplitude forced oscillations in roll are used, similar to test methods in a wind tunnel. The use of the first terms of the expansion in a Fourier transform series for aerodynamic loads simulated with a periodic change in the wing bank angle made it possible to extract the in-phase and out-of-phase aerodynamic derivatives. The out-of-phase aerodynamic derivative indicates the onset of wing rock at the angle of attack when this derivative changes sign from negative to positive. To predict the vortex breakdown phenomenon the dependence of rolling moment on bank angle (or sideslip) in static conditions is evaluated. The presence of strong non-linearity with onset of the positive slope at zero bank angle along with two asymmetric additional equilibria with negative slope serves as an indication of the so called pitch-fork bifurcation for wing equilibria [3, 12].

The paper is organised as follows. Section II presents the computational framework for CFD simulations using the URANS equations. The evaluation of wing-rock onset and prediction of the vortex breakdown along with flow visualisation of the vortex breakdown at high angles of attack are given in Section III. Results for the coupled fluid rigid body simulations of the wing rock motion at several angles of attack are presented in Section IV. Concluding remarks are given in Section V.

II. Computational framework

In this section, the adopted computational framework including the geometry of the wing and the virtual wind tunnel, along with insights on the overset grid generation techniques and numerical solver setup adopted for the simulations in this paper are discussed. Additionally, the Dynamic Fluid Body Interaction (DFBI) framework is briefly outlined.

A. Geometry and grid generation

A schematic setup for a free rotation in roll experiment with a delta wing with a sweep angle of 80 degrees is shown in Fig. 1, which is commonly used in experimental studies, and we will use it in numerical simulations in this paper. The geometric parameters of a considered 80-degree delta wing are: the root chord $c = 1.090$ m, the wing span $b = 0.3875$ m, the wing thickness 12.5 mm, the leading edges are rounded and the trailing edge is beveled [12].
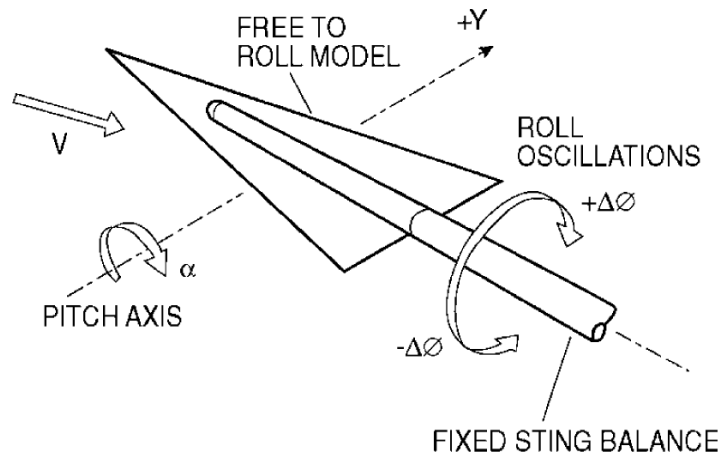

Fig. 1   Schematic view of the delta wing free-to-roll experiment [7].

The considered plan for numerical simulations involves both static and dynamic tests, which requires a body-fixed grid to be rotating around a prescribed center of rotation. Therefore, all simulations are conducted using an overset/chimera method which is very robustly implemented in Star-CCM+ CFD code [19]. This in turn means that the computational grid consists of two domains; the first domain is for the overset mesh consisting of the delta wing placed in a rectangular box hereafter named as "overblock zone". The second domain consists of the wind tunnel, hereafter named as the "background zone". The overblock zone's dimensions are carefully chosen as $1c_{ref}$ away in each direction from the center of rotation and $4c_{ref}$ away in the downstream direction. This allows to refine the near wake region in a more efficient way. One requirement for the adopted meshing approach with the overset method is that overset interface between the two zones should have similar spacing. This is to allow a smooth data interpolation of the flow variables between the two cell zones.

Several refinement strategies were considered in the initial mesh build up phase in order to make sure that the vortex
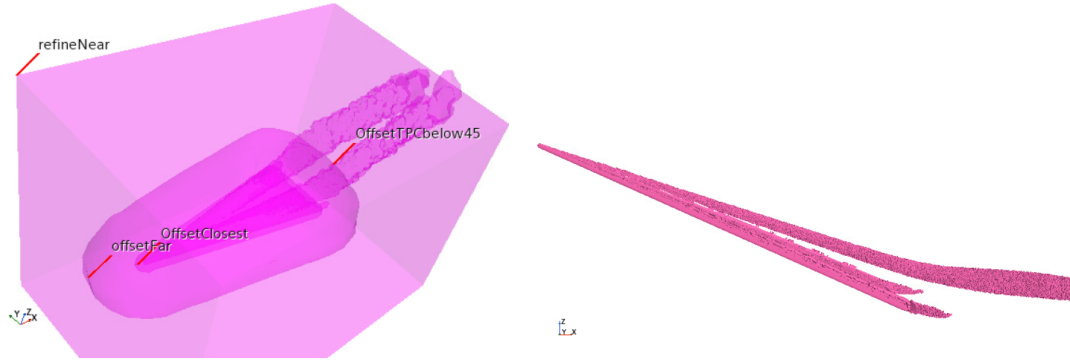
Fig. 2 Refinement strategies including extraction of the vortex location using iso-surface of total pressure coefficient for the 80 deg delta wing at $\alpha = 23°$.

dynamics, along with its strength and vortex pair interaction is accurately captured. Some of these strategies including the extraction of an iso-surface of the vortex based on total pressure coefficient from a coarse grid simulation along with volume offsets of the delta wing is shown in Fig. 2. An isometric view of the grid generated for $\alpha = 23°$ and section plane mesh view through the symmetry of the delta wing is shown in Fig. 3.

B. Numerical solver setup

The continuity, momentum and turbulence equations were solved in a segregated manner using the Algebraic Multi-Grid (AMG) solver with an inner tolerance of 0.001 solving the Matrix holding the discretized finite volume coefficients to an order of a minimum 3 decades. The V and F cycle approach was employed with 2 pre and post-sweeps in order to maximize convergence. For the multi-grid method, the restriction tolerance was kept at 0.9 and the prolongation tolerance was kept at 0.5. It was also necessary to employ some extent of under-relaxation of flow variables, especially due to the highly unsteady nature of the flow field. It was also necessary to exploit some degree of under-relaxation of the flow variables, especially for the high angle of attack and the wing rock simulations.
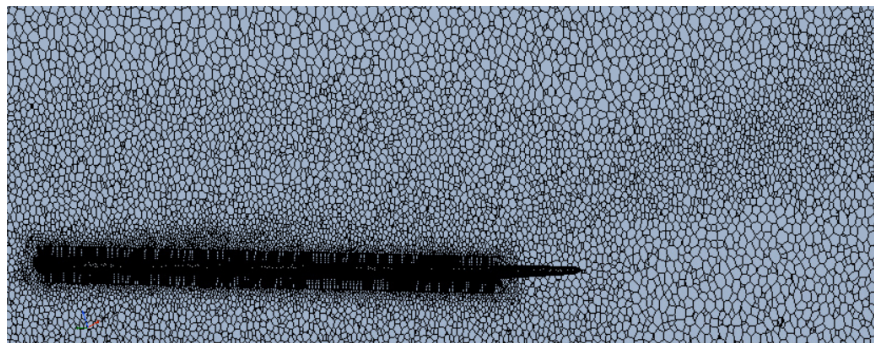

Fig. 3 Adopted grid for the 80 deg delta wing at $\alpha = 23°$.

Although the grids were intentionally constructed using a low wall $Y+$ approach, i.e. $Y+ < 1.0$, Star-CCM+ recommends using "All $Y+$ treatment". With this wall treatment method, boundary layers that meets the low $Y+$ criterion

are resolved using the low $Y+$ approach, and boundary layers that violate the low $Y+$ criterion are resolved using the high wall $Y+$ treatment method. The gradients of conservative flow parameters are solved with the second order of accuracy along with the Venkatakrishnan method [20], which excludes spurious oscillations in the flow field.

C. Mesh independence study at $\alpha = 23°$

A mesh independence study was conducted to determine the level of refinement required to obtain a grid independent solution. The computations were carried out at $\alpha = 23°$ and $\phi = 8.0°$. The obtained results for the lift coefficient against no of elements in the grid is shown in Fig. 4. The computational results obtained from URANS simulations in conjunction with Shear Stress Transport(SST) turbulence model [21] carried out at $\alpha = 23.0°$ and $\phi = 8.0°$ demonstrated that the obtained solution was independent of the grid beyond approximately 5.5 million elements.
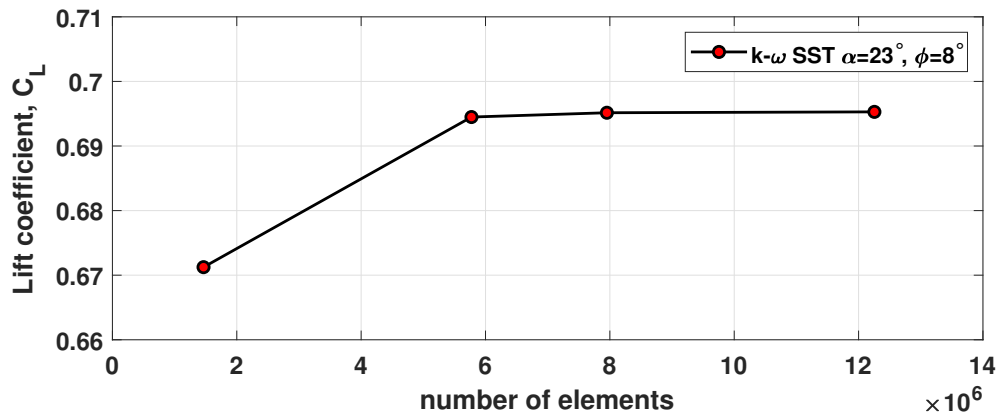

Fig. 4   Variation of the lift coefficient C_L with grid refinement at $\alpha = 23°$ and $\phi = 8.0°$.

D. Dynamic Fluid Body Interaction framework

The Dynamic Fluid Body Interaction (DFBI) framework allows a rigid body to under go free or constrained motion depending on either fluid forces acting on the body and/or external forces applied on the fluid body [17]. In this subsection the theory of the DFBI motion framework along with the setup used to for the free-to roll motion of the 80 degrees delta wing is briefly discussed.

The free motion of a body with a fixed mass and resultant forces acting in a local coordinate system can be expressed as:

$$M\frac{d\omega}{dt} + \omega \times M\omega = n \tag{1}$$

where M in Eqn. 1 is the tensor of the moments of inertia, ω is the angular velocity of the body and n is the resultant moment acting on the body [17].

The tensor of moments M can be expressed as below in Eqn. 2:

$$\begin{bmatrix} M_{xx} & M_{xy} & M_{xz} \\ M_{xy} & M_{yy} & M_{yz} \\ M_{xz} & M_{yz} & M_{zz} \end{bmatrix} \tag{2}$$

More precisely, here we are focused on the 1-DOF rotating motion which allows a free-to roll motion around the body x-axis of the wing. This type of motion can be prescribed as:

$$M \frac{\partial}{\partial t} \omega = n \tag{3}$$

A coupled system of equations for the wing free-to-roll motion under aerodynamic loads arising from this motion and predicted by the Unsteady Reynolds-Averaged-Navier-Stokes (URANS) equations is used to simulate the wing rock of an 80-degree delta wing at various given angles of attack. The obtained results of these simulation and their analysis are presented in Section IV. It should be noted that the friction moment in the wing bearings was considered negligible.

$$n_d = \frac{1}{2} \frac{M \omega^2}{\alpha - \alpha_{min}} \quad for \quad \alpha_{min} < \alpha < \alpha_{min} + \lambda \tag{4}$$

$$n_d = \frac{1}{2} \frac{M \omega^2}{\alpha_{max} - \alpha} \quad for \quad \alpha_{max} - \lambda < \alpha < \alpha_{max} \tag{5}$$

In Eqn. 4 and Eqn. 5 λ is the specified angular damping length. For this particular case study, the M_{xx} and other tensor components are dependent on the moment of inertia and they were obtained through the Star-CCM+ CFD code using the in-built functions. The obtained moment of inertia were based on a density of $1 kg/m^3$ and therefore were corrected to reflect the actual density of the delta wing in the experimental data presented in [12]. The 80 degrees delta wing in the experiment was made up of duralumin material. A summary of the wing dimensions and moment of inertia is presented in Table. 1.

Table 1   Reference data for the 80 degree delta wing)

Density of duralumin, ρ	$2780 kg/m^3$
Wing span, b	$0.3875m$
Root chord length, C_{root}	$1.090m$
Reference area, S_{ref}	$0.211m^2$
Moment Reference Center $CoM(m)$	$X = 0.727m, Y = 0, Z = -0.04161$
Moment of Inertia I	$I_{xx} = 0.04396848, I_{yy} = 0.4583386, I_{zz} = 0.5021236$

III. Prediction of the onset of wing rock and vortex breakdown

As the angle of attack increases, the leading edge vortices on the delta wing move vertically away from the surface and become more intense. In free wing motion, conical vortices lag behind in position and intensity compared to their state under static conditions. The delay of the vortices produces a destabilizing effect on the free movement of the wing, leading to the onset of oscillatory instability and self-excited steady-state oscillations, known as the wing rock phenomenon.

The wing rock roll amplitude reaches a maximum at a certain angle of attack and begins to decrease due to the onset of vortex breakdown occurring under static conditions [15]. Large-amplitude oscillations block the development of a complete vortex breakdown in great extent, but nevertheless extract less energy from the oncoming flow. Locally, the vortex breakdown transforms the wing rock motion creating a new type of motion in the form of "chaotic" low amplitude oscillations. Next, we discuss the computational indicators of the onset of large-amplitude oscillations caused by conical vortices and low-amplitude "chaotic" oscillations caused by the vortex breakdown.

A. Onset of wing rock

The free-to-roll motion of the wing is described by the following second order differential equation for one degree of freedom:

$$I_{xx}\ddot{\phi} = C_l(\phi, \dot{\phi}, t)\frac{\rho V^2}{2}Sb \tag{6}$$

where I_{xx} is the wing moment of inertia, ρ is the air density, V is the free stream velocity, S is the wing area, and b is the wing span. The rolling moment coefficient C_l depends on the wing motion parameters, the roll angle ϕ and the roll rate $\dot{\phi}$. The explicit dependence of the rolling moment coefficient C_l on time is introduced to reflect the delay and relaxation effects that occur in a vortex flow.

For prediction of the onset of wing rock motion the rolling moment coefficient $C_l(t)$ acting on the oscillating wing is simulated using the URANS equations. This computational simulation is identical to the experiment with forced-oscillation tests in a wind tunnel. During periodic variation of the roll angle $\phi(t) = \phi_s \sin(2\pi f t)$ the simulated rolling moment coefficient C_l after some transient process becomes also periodic in time with the same frequency $C_l(t) = C_l(t + 1/f)$. The computed process $C_l(t)$ approximated by the the first terms of the Fourier series allows to evaluate the in-phase and the out-of-phase aerodynamic derivatives:

$$C_l(t) = C_{l0} + C_{ls}\sin(2\pi f t) + C_{lc}\cos(2\pi f t) \tag{7}$$

7

Comparing 7 with the usual representation of the rolling moment coefficient in free motion:

$$C_l = C_{l0} + C_{l\beta}\beta + (C_{lp} + C_{l\dot{\beta}} \sin \alpha)\frac{pb}{2V}$$

$$p = \dot{\phi}, \quad \beta = \phi \sin \alpha, \quad \dot{\beta} = \dot{\phi} \sin \alpha$$

(8)

the in-phase and out-of-phase aerodynamic derivatives can be connected with the first terms of the Fourier series C_{ls} and C_{lc}:

$$C_{l\beta} \sin \alpha = \frac{1}{\phi_s}C_{ls}$$

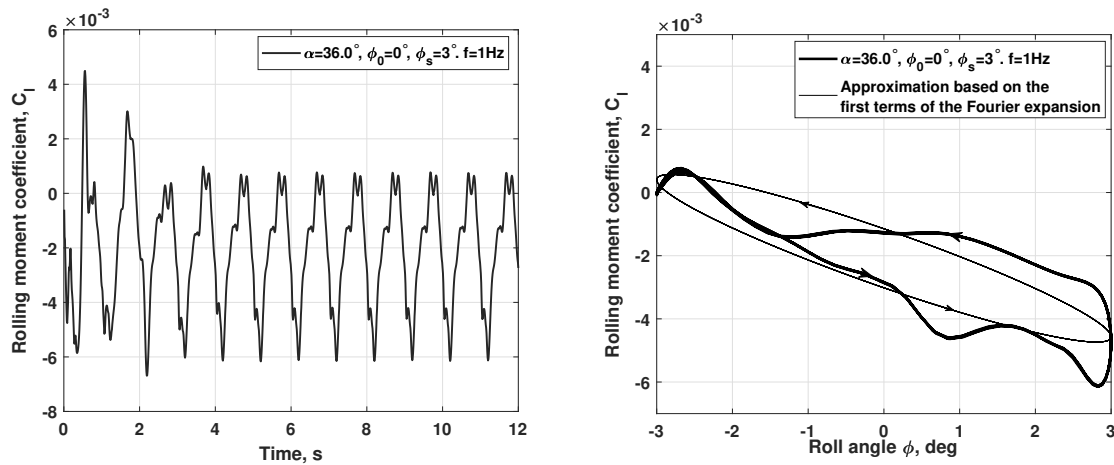$$C_{lp} + C_{l\dot{\beta}} \sin \alpha = \frac{V}{\phi_s \pi f b}C_{lc}$$

(9)

Fig. 5 **CFD simulation of the rolling moment coefficient C_l vs time during small amplitude wing oscillations in roll with amplitude $\phi_s = 3°$ at $\alpha = 36.0°$ (left plot). The elliptic approximation of the $C_l(\phi)$ cycle by the first harmonic of the Fourier expansion (right plot).**

The simulated process for $C_l(t)$ obtained in the roll forced-oscillations with amplitude $\phi_s = 3°$ at angle of attack $\alpha = 36°$ using the URANS equations is shown in Fig.5 (left plot). The Fourier series for the rolling moment coefficient $C_l(t)$ (7) is applied after the convergence to a periodic variation at $t > 6$s, which includes also high frequency oscillations produced by the vortex breakdown. The rolling moment coefficient C_l plotted versus the roll angle ϕ is shown in Fig.5 (right plot) in the form of a closed-loop trajectory with variation of time in anticlockwise direction. The first two terms of the Fourier series (7) approximate the simulated closed loop cycle for the rolling moment coefficient C_l by a harmonically equivalent ellipse. The slope of its major axis defines the in-phase aerodynamic derivative $C_{l\beta}$, while the size of the minor axis defines the out-of-phase aerodynamic derivative $C_{lp}^* = C_{lp} + C_{l\dot{\beta}} \sin \alpha$.

The obtained in-phase and out-of-phase aerodynamic derivatives are shown in Fig.6 for a range of angles of attack. The out-of-phase aerodynamic derivative C_{lp}^* in Fig. 6 (right plot) can be considered as an indicator of the oscillatory stability of the wing in its neutral position at $\phi = 0$. At low angles of attack $\alpha < 18°$ the out-of-phase aerodynamic
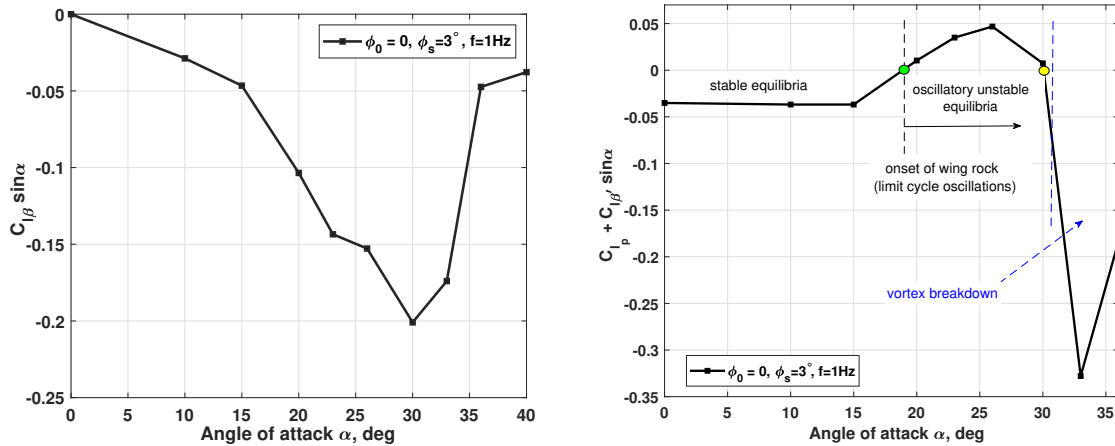
Fig. 6   Predicted in-phase and out-of-phase aerodynamic derivatives (the left and right plots, respectively) vs angle of attack.

derivative for an 80-degree delta wing remains negative $C_{lp}^* < 0$. This means that the wing is dynamically stable and will converge to its zero roll position after being given initial disturbances. The onset of oscillatory instability occurs at $\alpha = 18°$ when the out-of-phase derivatives becomes positive $C_{lp}^* > 0$ (green circle). Provisionally, the steady wing rock oscillations start at $\alpha = 18°$ with the amplitude growing with the absolute magnitude of the out-phase aerodynamic derivative characterising the intensity of the wing oscillatory instability. This type of transformation of the zero equilibrium of the wing during free rotation is described by the so-called supercritical Hopf bifurcation [3]. This bifurcation indicates the onset of an oscillatory instability of the equilibrium point with the simultaneous onset of a stable limit cycle characterizing the steady oscillations of the wing rock motion. The change of C_{lp}^* sign back to negative, making the equilibrium stable again, occurs at an angle of attack of $\alpha = 30°$ just before the start of the vortex breakdown. This type of transformation of the equilibrium of the wing during its free motion is described by the subcritical Hopf bifurcation [3], which generates a saddle-type limit cycle, the role of which is to separate two different attractors that characterize the dynamics of the wing with a vortex breakdown.

B. Onset of vortex breakdown

The static dependence of the rolling moment coefficient C_l on the roll angle ϕ can clearly show a sign of the onset of the vortex breakdown. At small angles of attack, the dependence $C_l(\phi)$ is almost linear with a negative slope $C_{l\phi} < 0$, which indicates the static roll stability of the wing. Intense conical vortices contribute to the "stiffness" of the wing at small bank angles, making the dependence $C_l(\phi)$ slightly concave and non-linear. The onset of vortex breakdown significantly changes the rolling moment coefficient $C_l(\phi)$. The neutral equilibrium of the wing with zero roll angle $\phi_e = 0$ becomes statically unstable $C_{l\phi} > 0$ with the simultaneous appearance of two additional asymmetric equilibria $\phi_e = \pm\phi_{vb}$ with a locally negative slope $C_{l\phi} < 0$. This type of transformation of equilibria is called a pitch-fork

bifurcation, which has the character of symmetry breaking [3].

The simulated and experimental dependencies of the rolling moment coefficient $C_l(\phi)$ for two settings of the angle of attack $\alpha = 23°$ and $\alpha = 36°$ are shown in Fig. 7. The agreement between the experiment [12] and the simulated dependencies obtained using the URANS equations at a slow sweep variation of the roll angle is good quantitatively and qualitatively. A slight positive shift in the experimental data may be due to the imperfection of the test model, interference with its support system, or the asymmetric breakdown of two vortices at $\alpha = 36°$ and $\phi = 0$.

Note that at an angle of attack $\alpha = 36°$, the computationally predicted dependence $C_l(\phi)$ is also slightly asymmetric with three equilibria determined by the zero points of the dependence of the rolling moment coefficient on the roll angle $C_l(\phi_i) = 0,\ i = 1, 2, 3.$The rolling moment coefficient at zero bank angle has a non-zero value $C_l(0) \approx 0.002$, which may indicate an asymmetric breakdown of the right and left vortices. An asymmetric breakdown of two vortices detached from the leading edges of the wing is clearly seen in Fig. 8 showing the visualization of the flow parameters when the wing is set to $\alpha = 36°$.
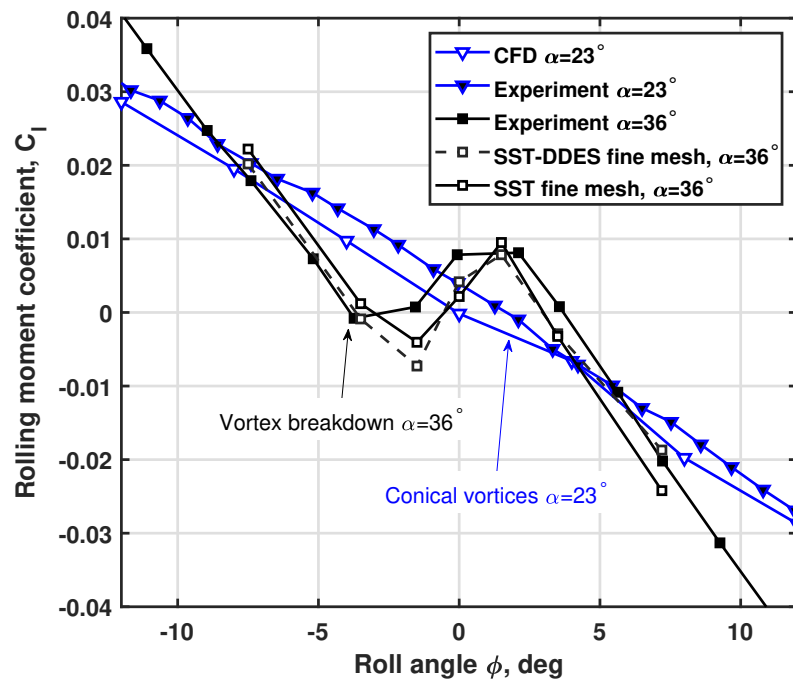

Fig. 7 **The rolling moment coefficient $C_l(\phi)$ dependencies for $\alpha = 23°$ and $\alpha = 36°$: simulated vs experimental results [12].**

For adequate simulation of a vortex flow with intense concentrated vortices, which are typical for small and medium angles of attack and the breakdown of vortices at high angles of attack, it is important to use a correctly created grid covering vortex cores and breakdown regions. A sufficiently fine grid provides realistic simulation of flow parameters with intense concentrated vortices and gives dependencies of the aerodynamic coefficients which are rather close to the
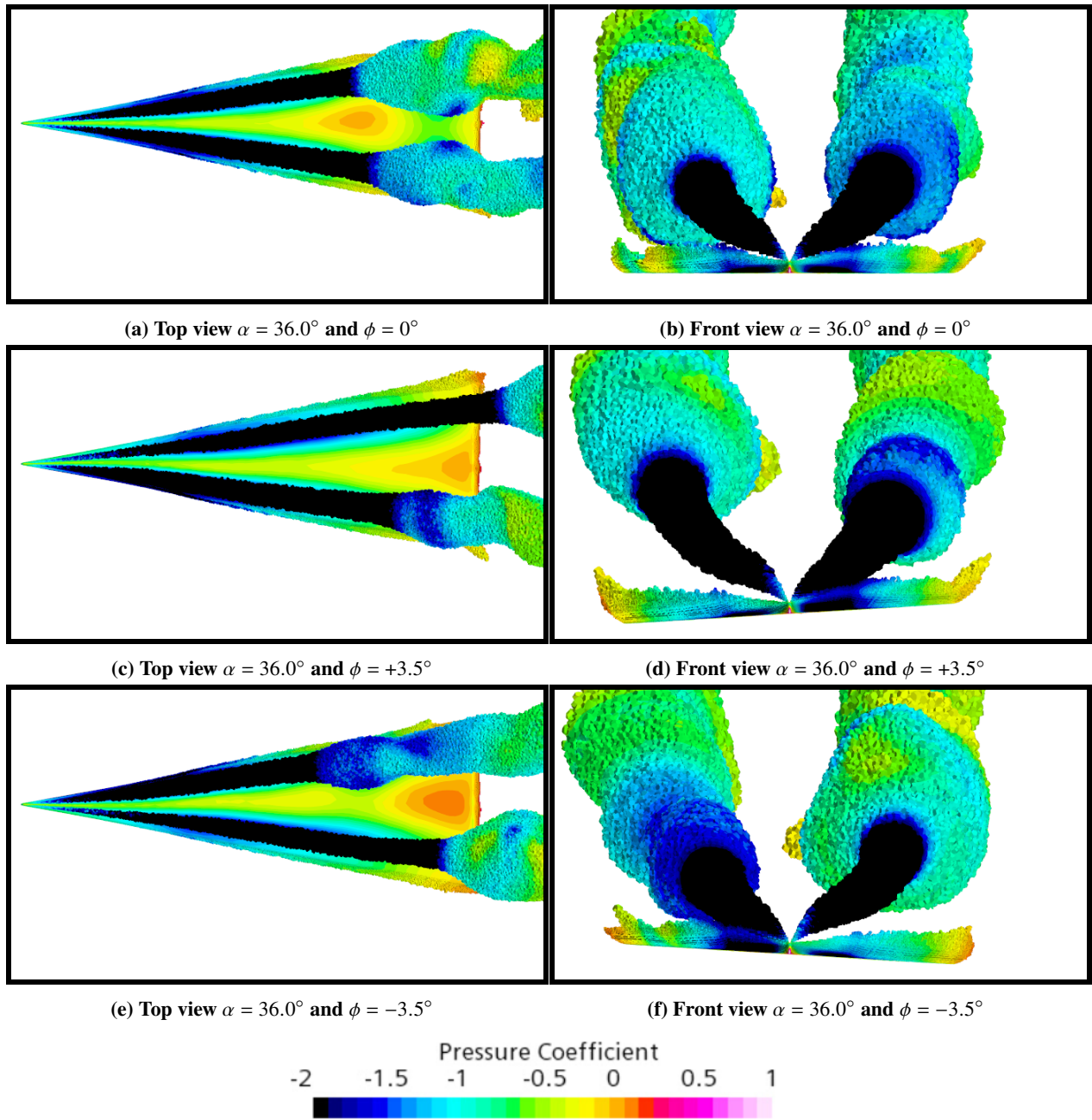
(a) Top view $\alpha = 36.0°$ **and** $\phi = 0°$

(b) Front view $\alpha = 36.0°$ **and** $\phi = 0°$

(c) Top view $\alpha = 36.0°$ **and** $\phi = +3.5°$

(d) Front view $\alpha = 36.0°$ **and** $\phi = +3.5°$

(e) Top view $\alpha = 36.0°$ **and** $\phi = -3.5°$

(f) Front view $\alpha = 36.0°$ **and** $\phi = -3.5°$

Fig. 8   Visualization of the vortex breakdown over an 80-degree delta wing at $\alpha = 36.0°$ **at various roll angles** $\phi = 0,\ 3.5°,\ -3.5°$**.**

11

experiment.

The simulation results with a medium mesh of approximately 5.5 million elements, which deemed sufficient in the mesh independence study at $\alpha = 23.0°$, failed to predict the nonlinear dependence for the rolling moment coefficient at $\alpha = 36.0°$ as shown in Fig. 7. To improve CFD predictions in this case the refined meshes were constructed ranging at approximately $8 - 9$ million elements with particular focus on refining the vortex cores using a total pressure coefficient threshold. This improvement allowed to capture the same nonlinear trends in the rolling moment coefficient as in the experiment using both the k-ω SST URANS approach and the k-ω SST Delayed Detached Eddy Simulation (DDES) approach.

A visualization of the vortical flow field shown in Fig. 8 was carried using the inbuilt threshold functions of Star-CCM+ to plot the contours of the pressure coefficient on the surface of the wing and in its immediate vicinity. It can be seen from the visualized flow field that the presence of a non-zero rolling moment coefficient at zero bank angle $\phi = 0$ is due to the asymmetric breakdown of the wing vortices.

Fig. 8 also presents the visualised flow field for simulated results obtained at non-zero bank angles $\phi = -3.5°$ and $3.5°$. At $\phi = +3.5°$ the breakdown of the left vortex on the wing occurs much further upstream compared to the breakdown of the right vortex. On the contrary, for $\phi = -3.5°$ the breakdown of the left vortex on the wing occurs much further downstream compared to the right vortex. It is also seen that although the absolute value of the bank angle is the same, the location of the right vortex breakdown at $\phi = -3.5$ occurs almost at half the length of the chord, and the left vortex separation at $\phi = 3.5$ occurs close to the trailing edge.

Such a nonlinear behavior of the vortex breakdown phenomenon in Figs. 8 can be the main cause of non-linear trends in the dependencies of aerodynamic loads at high angles of attack, leading to the onset of aerodynamic asymmetry and static hysteresis phenomena. Some evidence of this can be seen in the dependence of the aerodynamic rolling moment shown and discussed earlier in Fig. 7.

IV. Coupled fluid rigid body simulation of the wing rock motion

Simulation of the free-to-roll motion of the wing is carried out using a coupled system of equations describing the movement of the wing under the action of aerodynamic loads, predicted by simultaneously solving the Unsteady Reynolds-Averaged-Navier-Stokes (URANS) equations. The results of such simulation and their analysis are presented in this section. The aerodynamic loads including distributed pressure and viscous forces are evaluated at each time step and used to transform the body-fixed grid in the overset region according to the tensor of moment of inertia. The friction moment in the wing bearings is considered negligible.

A. Wing rock simulations at various angles of attack

Simulation of wing rock motion was performed for a number of angle of attack settings $\alpha = 15°, 20°, 23°$ and $36°$ to illustrate different types of wing behaviour predicted based on the out-of-phase derivative C_{lp}^* (Fig. 6). The simulation process for $\alpha = 15°$ in the form of time history $\phi(t)$ and the phase portrait $\dot{\phi}$ vs ϕ is shown in Fig. 9. The motion of the wing is stable, rather fast damping of the oscillation amplitude and convergence to the neutral equilibrium state $\phi_e = 0$ are observed. This type of behavior correlates well with the predicted value of the aerodynamic derivative $C_{lp}^* = -0.037$ for $\alpha = 15°$. At an angle of attack of $\alpha = 20°$, the wing motion is oscillatory unstable due to the sign change of the aerodynamic derivative $C_{lp}^* = 0.01$ to positive. The process for this case, shown in Fig. 10, has a very slow increase in oscillation amplitude without convergence to a steady wing motion over a given time interval. At a larger angle of attack $\alpha = 23°$, the intensity of oscillatory instability $C_{lp}^* = 0.035$ is more than three times higher than at $\alpha = 20°$. The simulated time history and phase portrait for this angle of attack are shown in Fig. 11. The increase in amplitude occurs more intensively with saturation in steady-state oscillations over a time interval of 20 seconds. The amplitude of the steady oscillations of the wing is approximately 40 degrees.

The time history for the rolling moment coefficient and the twisted loop showing dependence of the rolling moment coefficient versus roll angle for $\alpha = 23°$ are presented in Fig. 12. Variation of the rolling moment coefficient $C_l(\phi)$ in the form of a twisted loop in Fig. 12 (on the right) corresponds to the end of the oscillatory process with practically maximal amplitude of a saturated wing rock motion. The section in the middle of the loop with the passage of time in a clockwise direction (energy extraction from the flow) is compensated by two sections at both ends of the loop with a counterclockwise course of time (energy is dissipated from the wing), which indicates the balance of energy for the interval of one oscillation cycle.
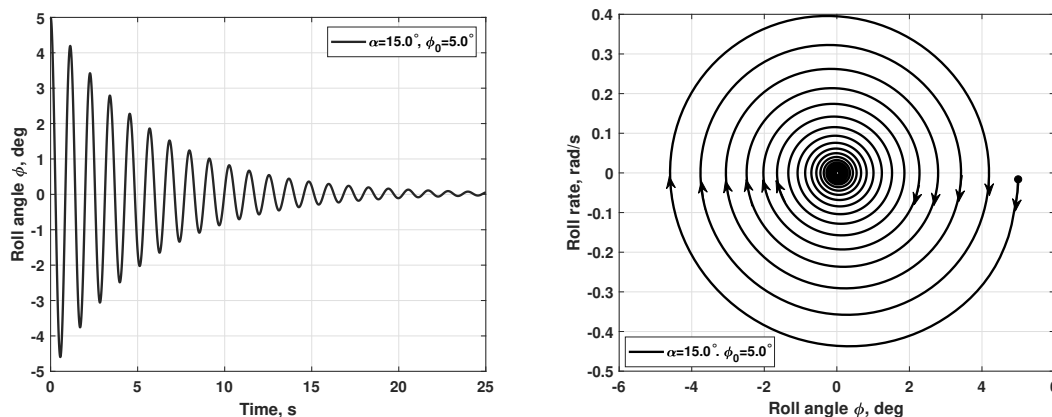

Fig. 9 Simulated time history (left graph) and phase portrait (right graph) of the 80-degree delta wing in free-to-roll rotation at angle of attack $\alpha = 15.0°$ with initial roll angle $\phi_0 = 5.0°$.

The free roll oscillations of the wing change significantly at $\alpha = 36°$ due to the onset of the vortex breakdown. Regular oscillations of large amplitude still remain, but small amplitude oscillations appear additionally, which have an
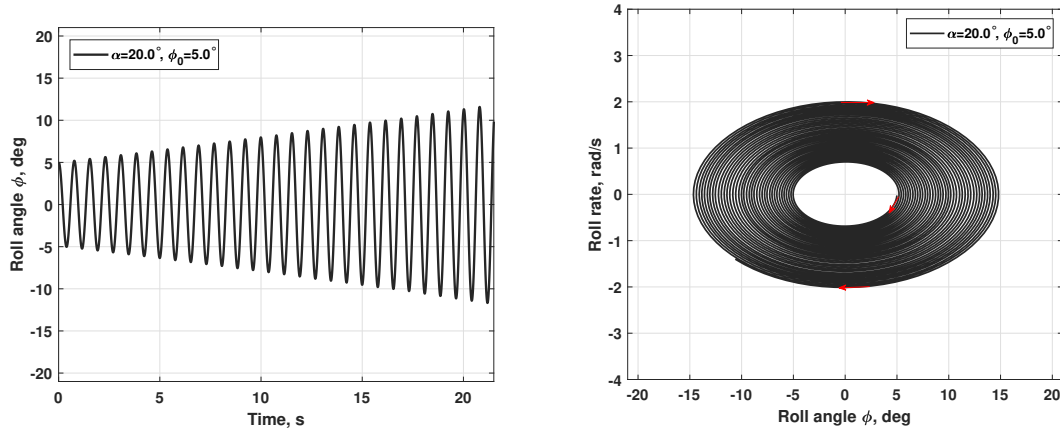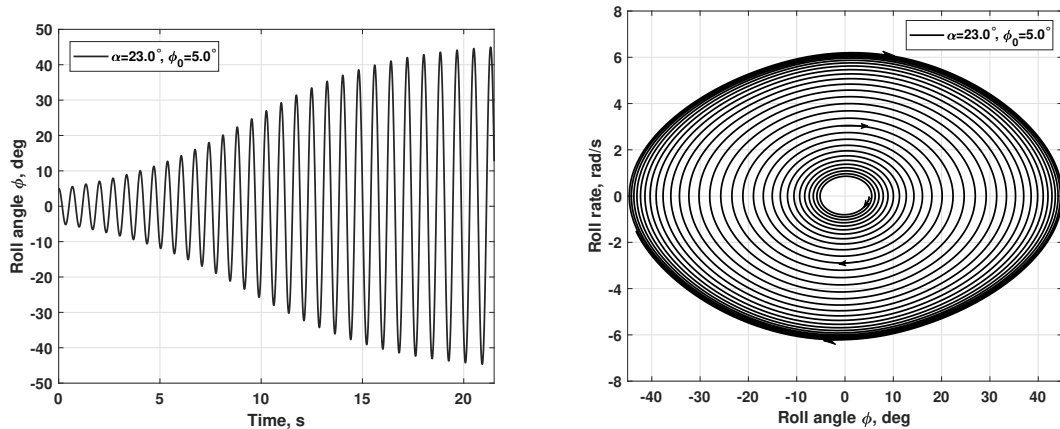
Fig. 10 Simulated time history (left graph) and phase portrait (right graph) of the 80-degree delta wing in free-to-roll rotation at angle of attack $\alpha = 20.0°$ with initial roll angle $\phi_0 = 5.0°$.

Fig. 11 Simulated time history (left graph) and phase portrait (right graph) of the 80-degree delta wing in free-to-roll rotation at angle of attack $\alpha = 23.0°$ with initial roll angle $\phi_0 = 5.0°$.

irregular or "chaotic" character. The excitation of one of these types of motion depends on the initial roll angle.

"Chaotic" oscillations are generated between two equilibrium points opposite in sign, arising after the breakdown of the vortices. These two equilibria $\phi_e = \pm 3.5°$ (see Fig. 7) are also oscillatory unstable, but due to the increase in amplitude around the one equilibrium point, the wing is attracted to the opposite equilibrium point with subsequent repulsion back. This process creates a movement of the wing, which has a "chaotic" character. A more detailed analysis of this mechanism can be found in [22].

These "chaotic" oscillations of the wing are very sensitive to any numerical changes introduced into the system, for example, to the integration time step, initial conditions, etc. Simulation of "chaotic" oscillations of the wing, initiated at the same initial roll angle $\phi_0 = 8°$, but with different time integration steps $t = 0.01s$ and $t = 0.005s$ are shown in Fig.13 and Fig. 14, respectively. A coupled flow solver with inviscid flux approximated by Roe Flux Difference Splitting (Roe
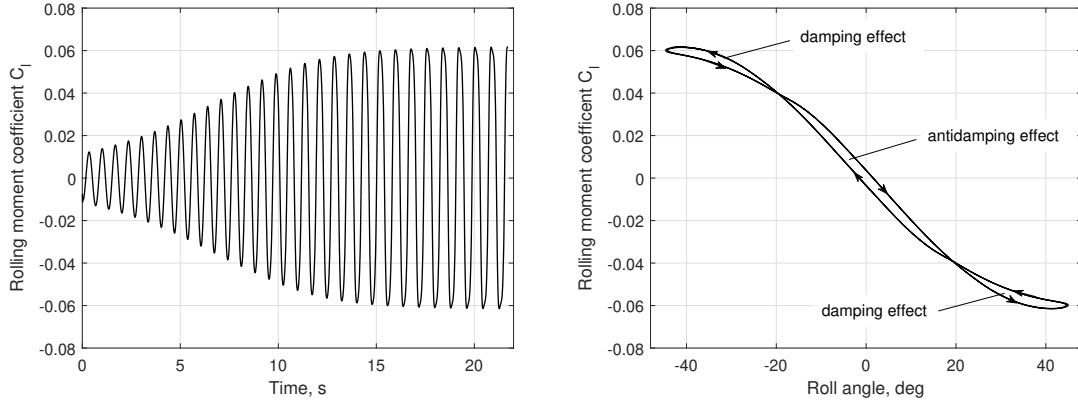
Fig. 12   The rolling moment coefficient vs time (left graph) and the rolling moment coefficient vs roll angle (right graph) of the 80-degree delta wing in free-to-roll rotation at angle of attack $\alpha = 23.0°$ with initial roll angle $\phi_0 = 5.0°$.

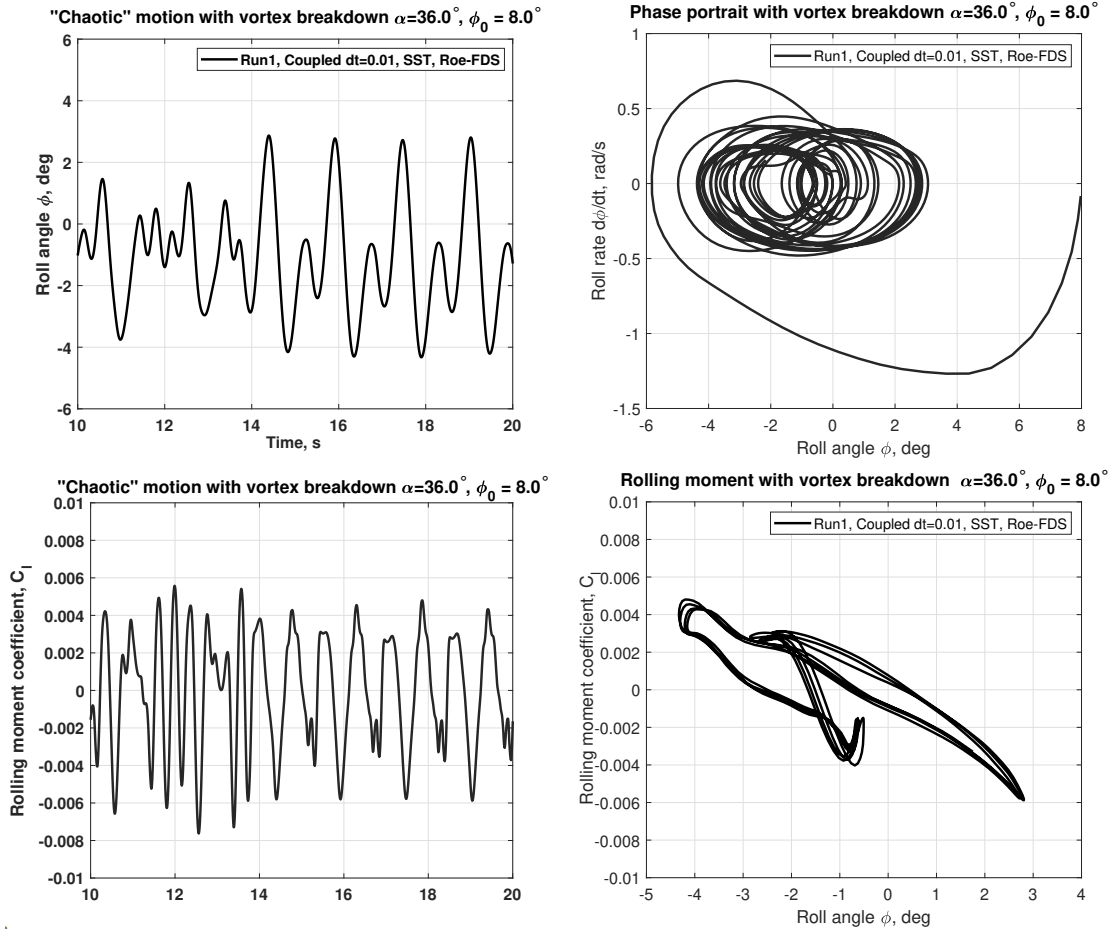**Fig. 13   Simulation results for "chaotic" free-to-roll oscillations of the 80-degree delta wing at $\alpha = 36.0°$ with initial roll angle $\phi_0 = 8.0°$: roll angle ϕ time history (upper left plot), phase portrait (upper right plot), rolling moment coefficient C_l time history (lower left plot) and C_l vs roll angle ϕ (lower right plot). Time step used in simulation $dt = 0.01 s$.**
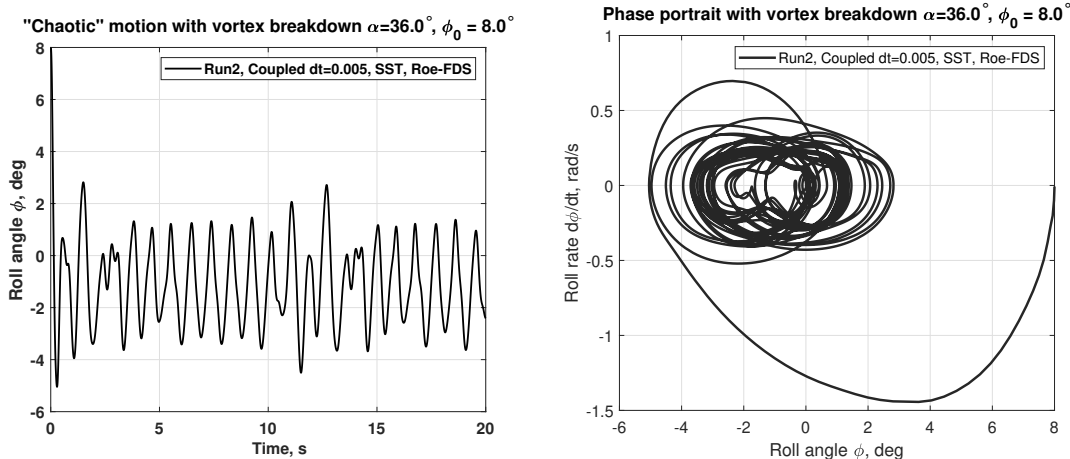
Fig. 14   Simulation results for "chaotic" free-to-roll oscillations of the 80-degree delta wing at $\alpha = 36.0°$ with initial roll angle $\phi_0 = 8.0°$: roll angle ϕ time history (left plot), phase portrait (right plot). Time step used in simulation $dt = 0.005s$.

FDS) was used in both simulations. It is clearly seen that the temporal characteristics of the roll angle and the phase portrait in these two simulations are somewhat different, but retain their chaotic nature and magnitude of the amplitudes.

When the initial roll angle is increased to $\phi_0 = 24°$ the wing converges to the regime with large amplitude oscillations with maximum roll angle of $\phi_{max} \approx 40°$ as it was at $\alpha = 23°$. Fig. 15 shows these simulations in comparison with some experimental results from [12]. The time history of the roll angle $\phi(t)$ (the upper graph) is very close to the experimental process shown by circle markers both in the amplitude and periodic time. The change in the rolling moment coefficient C_l during these oscillations in comparison with the static dependence of the rolling moment coefficient on the roll angle, shown earlier in Fig. 7, indicates that vortex breakdown does not occur during large amplitude oscillations. It is possible that due to the high roll rates in the mode with large amplitude oscillations, the flow regimes change, preventing the occurrence of vortex breakdown phenomena.

Fig. 16 (upper graph) shows a phase portrait combining large amplitude oscillations and a "chaotic" small amplitude oscillation mode, which were obtained in the presented above CFD simulations for two different initial conditions for the bank angle. On fig. 16 (lower graph) shows a similar phase portrait based on experimental data from [12]. One can see that there is a very good quantitative and qualitative agreement beteween the CFD predicted wing roll behaviour and the experimental observations which clearly demonstrate two stable modes of the wing roll oscillations of a 80-degree delta wing at $\alpha = 36°$. The excitation of the low-amplitude "chaotic" oscillations with vortex breakdown and regular large-amplitude oscillations without vortex breakdown depends on the system initial motion parameters.

V. Conclusions

Numerical simulations of the free motion in roll of an 80-degree swept delta wing was performed using a state-of-the-art CFD methods and the chimera/overset mesh technique in combination with Dynamic Fluid Body Interaction
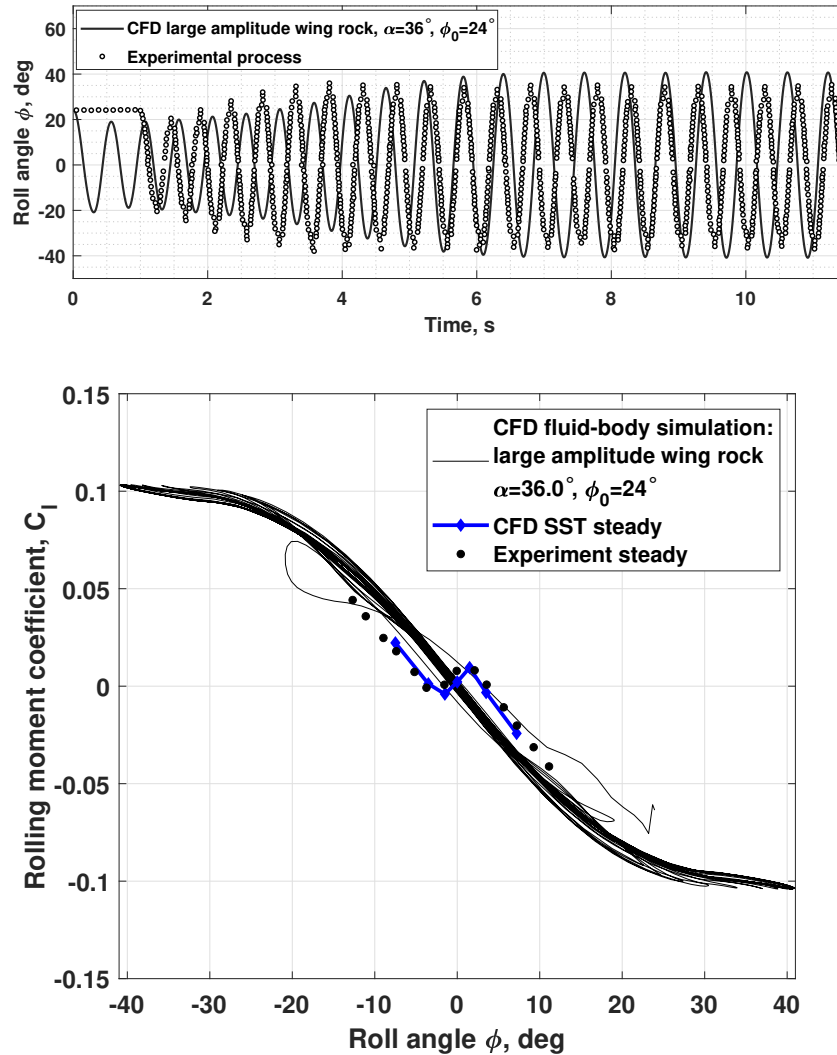
Fig. 15 **Computational results for the rolling moment coefficient** C_l **vs roll angle** ϕ **(top) and roll angle time history (bottom) during wing rock motion at** $\alpha = 36.0°$ **with a release angle of** $\phi_0 = 24.0°$**.**

(DFBI). The simulation results allowed us to draw the following conclusions:

- A higher resolution grid is needed to accurately predict nonllinear aerodynamic loads acting on the wing at small and medium angles of attack with intense conical vortices and vortex breakdown at high angles of attack. The mesh refinement is required for the cores of the vortices and regions with vortex breakdown.

- The in-phase and out-of-phase aerodynamic derivatives obtained in CFD simulations, in a manner similar to those obtained in forced oscillation tests in a wind tunnel, can be effectively used to predict the onset of steady-state roll oscillations.

- Numerical simulations revealed two different modes of wing oscillations in roll, at high angle of attack $\alpha = 36°$, which depends on the initial motion parameters. The low amplitude "chaotic" wing oscillations are strongly affected by the breakdown of wing vortices and the regular large-amplitude oscillation extend existence of conical
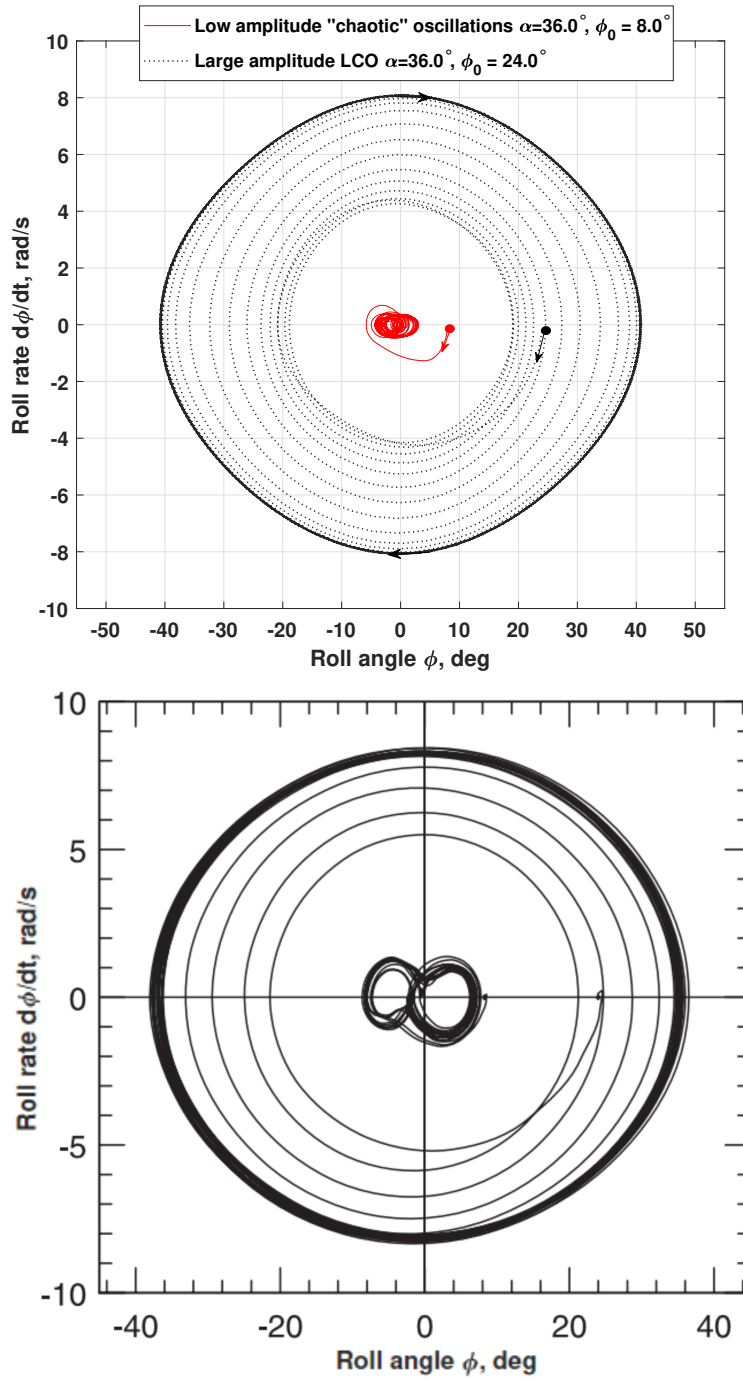
17

Fig. 16   Simulated (upper plot) and experimental (lower plot) phase portraits for $\alpha = 36°$ with two trajectories for initial conditions $\phi_0 = 8°$ and $\phi_0 = 24°$.

vortices and block the vortex breakdown. The predicted two wing oscillation modes are in a very good quantitative and qualitative agreement with the available experimental results.

- The performed CFD simulation of the multi-mode nonlinear dynamics of a delta wing with a sweep angle of 80 degrees during free roll rotation gave a positive agreement with the entire set of experimental data and made it

18

possible to validate an overset grid approach.

References

[1] K. Orlik-Ruckermann. Aerodynamics aspects of aircraft dynamics at high angles of attack. Journal of Aircraft, 20(9):737–752, - 1983. .

[2] N. Abramov, M. Goman, A. Khrabrov, and B. Soemarwoto. Aerodynamic modeling for poststall flight simulation of a transport airplane. Journal of Aircraft, 56(4):1427–1440, April 2019. doi:https://doi.org/10.2514/1.C034790.

[3] M. Goman, G. I. Zagainov, and A. V. Khramtsovsky. Application of bifurcation methods to nonlinear flight dynamics problems. Progress in Aerospace Sciences, 33(9-10):539–586, 1997. doi:https://doi.org/10.1016/S0376-0421(97)00001-8.

[4] L.T. Nguyen, L. Yip, and J.R. Chambers. Self-induced wing rock of slender delta wings, AIAA Paper 81-1883, AIAA Atmospheric Flight Mechanics Conference, Albuquerque, NM. August 1981. .

[5] L.E. Ericsson. Wing rock analysis of slender delta wings, review and extension. Journal of Aircraft, 32(6):1221–1226, Nov.-Dec. 1995.

[6] D. Levin and J. Katz. Self-induced roll oscillations of low-aspect-ratio rectangular wings. Journal of Aircraft, 29(4):698–702, July-Aug. 1992.

[7] Joseph Katz. Wing/vortex interactions and wing rock. Progress in Aerospace Sciences, 35:727–750, 1999. .

[8] A. Arena. An experimental and computational investigation of slender wings undergoing wing rock. , PhD Thesis University of Notre Dame, April 1992. .

[9] A.S. Arena and R.C. Nelson. Experimental investigations on limit cycle wing rock of slender wings. Journal of Aircraft, 31(5):1148–1155, Sept-Oct. 1994.

[10] I Gursul. Unsteady flow phenomena over delta wings at high angle of attack. AIAA, 32(2):225–231, February 1994. doi:https://doi.org/10.2514/3.11976.

[11] C Lambert and I. Gursul. Characteristics of fin buffeting over delta wings. Journal of Fluids and Structures, 19(3):307–319, April 2004. doi:https://doi.org/10.1016/j.jfluidstructs.2003.12.007.

[12] A. Khrabrov, K. Kolinko, O. Miatov, and A. Zhuk. Delta wing unsteady aerodynamic characteristics at high angles of attack during small and large amplitude forced oscillations. Technical report, TsAGI-DERA: MSS/4C3430, 1998.

[13] Elizabeth M. Lee-Rausch and John T. Batina. Conical Euler Analysis and Active Roll Suppression for Unsteady Vortical Flows About Rolling Delta Wings. , NASA Technical Paper 3259, 1993. .

[14] K. Badcock and M.R. Allan. Fast Prediction of Wing Rock Onset Based on Computational Fluid Dynamics. Int. Forum on Aeroelasticity and Structural Dynamics, pages 1–19, 2005. http://www.cfd4aircraft.com/Publications/cd-2006/papers/Wingrock-IFASD05.pdf.

[15] Robeet C. Nelson and Alain Pelletier. The unsteady aerodynamics of slender wings and aircraft undergoing large amplitude maneuvers. Progress in Aerospace Sciences, 39:185–248, 2003. .

[16] M. Hirano and K. Miyaji. Numerical analysis of the free-to-roll wing rock motion by the fluid dynamics-flight dynamics coupling. , 24th internation congress of the aeronautical sciences, August 2004. .

[17] Siemens Digital Industries Software. Simcenter STAR-CCM+, version 2021.1, Siemens 2021.

[18] M. Sereez, N. Abramov, and M. Goman. Investigation of Aerodynamic Characteristics of a Generic Transport Aircraft in Ground Effect Using URANS Simulations. , The Royal Aeronautical Society: Applied Aerodynamics Conference, September 2022. .

[19] Siemens Digital Industries Software. Simcenter STAR-CCM+ User Guide, version 2021.1. In Adaptive Mesh Refinement for Overset Meshes, pages 3067–3070. Siemens, 2021.

[20] V. Venkatakrishnan. On the accuracy of limiters and convergence to steady-state solutions. 31st Aerospace Sciences Meeting, AIAA, June 1993. doi:`https://doi.org/10.2514/6.1993-880`.

[21] F. R. Menter. Two-equation eddy-viscosity turbulence models for engineering applications. AIAA, 32(8), 1994. doi:`https://doi.org/10.2514/3.12149`.

[22] M.G. Goman, A.N. Khrabrov, and A.V. Khramtsovsky. Chaotic Dynamics in a Simple Aeromechanical System. , in the Book "Fractal Geometry. Mathematical Methods, Algorithms, Applications", Horwood Publishing Ltd, 2002. .